This is a repository copy of *Numerical modelling of FRP-reinforced masonry walls under in-plane seismic loading*.

White Rose Research Online URL for this paper:
http://eprints.whiterose.ac.uk/109880/

Version: Accepted Version

Numerical modelling of FRP-reinforced masonry walls under in-plane seismic loading

Si Zhang[a,b,c], Dongmin Yang[b,*], Yong Sheng[b], Stephen W. Garrity[b], Lihua Xu[a]

[a] **School of Civil Engineering, Wuhan University, Wuhan 430072, China.**

[b] **School of Civil Engineering, University of Leeds, LS2 9JT, UK.**

[c] **CITIC General Institute of Architectural Design and Research Co., Ltd, Wuhan, 430014, China.**

Abstract: This paper describes the development of Finite Element (FE) models for the study of the behaviour of unreinforced and Basalt Fibre Reinforced Polymer (BFRP) externally reinforced masonry walls under the action of in-plane seismic loading. Validated against experimental tests, the FE models were used to accurately predict the shear strength and reflect damage progression in multi-leaf masonry walls under in-plane cyclic loading, including the propagation of cracks beneath the BFRP reinforcement. The models have the potential to be used in practice to predict the behaviour and shear capacity of unreinforced and FRP-reinforced masonry walls.

Key words: **Masonry walls; FRP; FE modelling; Cohesive element; Seismic performance; Shear capacity**

1. Introduction

In the past few decades, the use of fibre reinforced polymers (FRP) to strengthen masonry structures has become increasingly popular. Experimental studies have shown that FRP strengthening technology can enhance the shear resistance and seismic capacity of masonry structures [1-4]. Of the different types of FRP that have been used to strengthen existing structures, basalt fibre reinforced polymer (BFRP) has proved to be one of the most cost effective [4, 5].

* Corresponding author. Email: d.yang@leeds.ac.uk; Tel: +44 (0)113 3432291.

22 The mechanical behaviour of masonry is much more complex than that of concrete and steel, largely

23 because masonry consists of two distinct components, namely the masonry units and the mortar

24 joints as shown in Fig.1 (a). As a result masonry structures are inhomogeneous containing many

25 discontinuities. This partly explains why, in experimental studies, the results from the testing of two

26 identically built masonry walls are not identical [6]. The degree of complexity is heightened further

27 by the inherent variations in the materials and variations in workmanship. Further difficulties exist

28 when testing masonry structures in the laboratory such as the accurate detection and monitoring of

29 cracks and their propagation beneath and around external reinforcement. Computational modelling

30 technology provides a valid and useful alternative to experimental studies. To date, numerical

31 models have been developed based on different theories such as the Finite Element Method (FEM)

32 [7-22] and the Distinct and Discrete Element Methods (DEM) [11, 23-25]. Of these, FEM-based

33 models and software are the most popular and widely available. FEM modelling strategies can be

34 broadly classified into three categories [22]: micro-scale, meso-scale and macro-scale modelling.

(a)   (b)   (c)
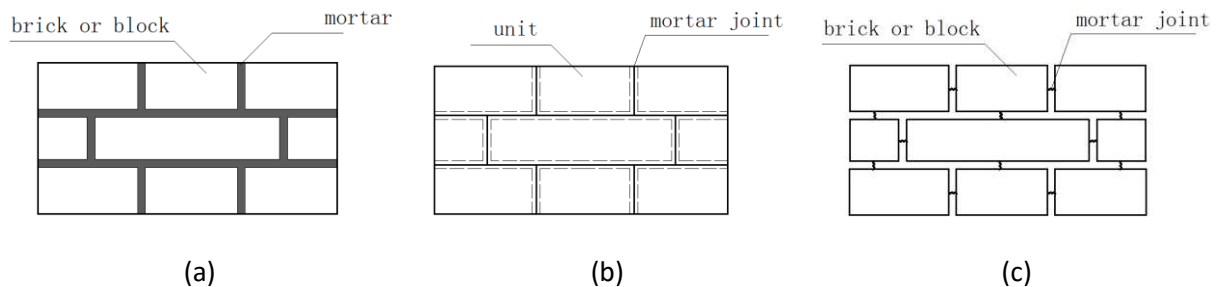
35 Figure 1.Modelling of masonry: (a) real masonry; (b) meso- scale modelling with interfaces; (c) meso-

36   scale modelling with springs.

37 Macro-scale modelling regards all the components of masonry as a single continuum in which solid

38 elements or shell elements are widely adopted [7-12]. The constitutive material models are initially

39 simplified to be homogeneous and isotropic and concrete damage plasticity and concrete smeared

40 cracking are commonly used [10-12]. Some researchers have attempted to adapt the constitutive

41 material models to represent the orthotropic feature of masonry. In the modelling by Dhanasekar

42 and Haider [9], the material properties of head (perpend) and bed joints are considered separately.

43   Alternatively, with the use of homogenisation technology, a series of material models have been

44   developed where the behaviour of masonry is expressed by macro or average stresses and strains.

45   This concept was originally proposed by Lourenço in 2002 and was subsequently validated under

46   various loading conditions [13-15]. Essentially, because of the reduced computational cost and

47   material parameters, macro-scale modelling is suitable for large-scale structural analysis. However,

48   macro modelling does not always simulate some important mechanical behaviour of the interfaces

49   between the masonry units and the mortar and it fails to capture the cracking pattern in mortar

50   directly.

51   Unlike macro-scale modelling, the masonry units, mortar joints and the unit-mortar interfaces are

52   considered separately in micro-scale modelling. In this case, the masonry units and mortar are

53   modelled with real thickness and are assigned corresponding material properties, while zero

54   thickness unit-mortar interfaces are sandwiched between the masonry units and the mortar. With

55   the assumption that the interface is a mixture of units and mortar, Rekik and Lebon [16] used an

56   homogenisation approach to obtain the mechanical properties of the unit-mortar interface.

57   Although this approach seems to be straightforward, the large number of elements used in the

58   analysis requires the use of extensive computational resources. Also, the material properties of the

59   unit-mortar interfaces are difficult to measure experimentally which creates difficulties when

60   validating the complete model. Therefore, with micro-scale models it is often assumed that the

61   masonry units and/or the mortar joints remain elastic, which tends to mean that the modelling

62   strategy can only be used for small masonry specimens such as masonry shear triplets [12, 16].

63   Meso-scale models are routinely termed simplified micro-scale models. Similar to micro-scale

64   models, they can provide an insight into damage evolution in masonry. However, without the

65   masonry unit-mortar interface, the distinction between failure occurring at the unit-mortar interface

66   and within the mortar will be lost. Meso-scale modelling only allows cracks to initiate in the mortar

67   joints and to propagate along the well-defined pattern of lines. This modelling method is based on

68 observations from the experimental testing of masonry [26] and has been proved to be effective for

69 modelling some large elements of masonry construction [17, 18].

70 Meso-scale models can be divided into two groups; those that take into account de-bonding or slip

71 failures that occur between the masonry units and the mortar joints and those that do not. The

72 former can be achieved by coupling the coordination of nodes in the units and mortar joints in all

73 degrees [19], while the latter models normally use contact or some special-purpose elements

74 (interface elements, springs, *etc*.) to replace the mortar [17, 18, 20-22]. In the case of interface

75 elements or contacts, the masonry units are expanded in size by a half mortar joint thickness to

76 create a new component while the mortar joints are simplified as zero-thickness interface elements

77 or contacts (Fig1(b)). Alternatively, as shown in Fig.1(c), the masonry units are assigned their real

78 geometry and the distance between them represents the thickness of the mortar joints in real

79 construction [20]. It is also common to simulate the units using deformable solid elements when

80 interface elements or contacts are applied, while springs are used in conjunction with rigid elements

81 for bricks. Hence, it is evident that not all meso-scale models are the same.

82 ABAQUS finite element software provides several kinds of interface elements including cohesive

83 elements which are used widely to simulate de-bonding or sliding [27]. Cohesive elements can be

84 classified as element-based cohesive elements and surface-based cohesive elements, both of which

85 can reproduce the behaviour of mortar joints. In Ref. [22], element-based cohesive elements are

86 assigned with a user-defined constitutive model to represent the cyclic behaviour of mortar; the

87 unreinforced masonry models are validated under monotonic and cyclic loadings. The model in Ref.

88 [21] is set up with surface-based cohesive elements, but is only validated under monotonic loading.

89 Similar to a contact model, the material properties of surface-based cohesive elements are specified

90 as interaction features and the status of closure or opening between elements is checked at the

91 beginning of each step in the applied load. As a result, models using surface-based cohesive

92 elements tend to have a high risk of convergence problems and require larger computational

93 resources, especially under cyclic load simulations. For these reasons, the element-based cohesive

94 element is used for the modelling of masonry subjected to both monotonic and cyclic loading

95 described in this paper.

96 Although 2-D models are widely adopted for single leaf masonry wall construction [11, 16, 28, 29],

97 3-D models using non-linear analysis are preferred for masonry with more complex arrangements of

98 masonry units. Until relatively recently, a great deal of research effort has been devoted to the study

99 of single-leaf masonry, whereas numerical studies of the behaviour of multi-leaf walls and other

100 more complex forms of construction is less common. More complex forms of masonry are usually

101 analysed using either FEM or a 3-D FE kinematic limit analysis. The model proposed by Burnett et al

102 [17] is applied to masonry walls using contact in LS-DYNA. In Ref. [20] using non-linear spring

103 elements to represent mortar joints, meso-scale models of masonry walls are used in ABAQUS. In

104 the model developed by Macorini and Izzuddin [30], novel 2-D interface elements and 3-D solid

105 elements are used to account for different masonry unit arrangements. These models, validated

106 under monotonic loading, permit the study of masonry walls with complex geometry and unit

107 bonding patterns. However, due to the high computational demand and a lack of a suitable

108 representative constitutive material model for unloading and reloading, few models of this type

109 have been validated under cyclic load conditions.

110 In this paper, a meso-scale masonry model is developed in ABAQUS with element-based cohesive

111 element to simulate both unreinforced and FRP-strengthened masonry walls subjected to

112 monotonic and cyclic loading. In Section 2, the unreinforced and FRP-reinforced numerical models

113 with cohesive elements are described and the material constitutive model for cohesive elements is

114 explained. The laboratory testing of full-scale unreinforced walls and walls with externally bonded

115 BFRP reinforcement under cyclic loading is described in Section 3. Section 4 describes convergence

116 studies, the model validation and then the monotonic and cyclic load simulations. The results from

117 the computational model are discussed and compared with the experimental results and the

118   guidance provided in the Chinese and European codes for masonry [39, 46]. The principal

119   conclusions from the research are presented in Section 5.

2. Description of the finite element model

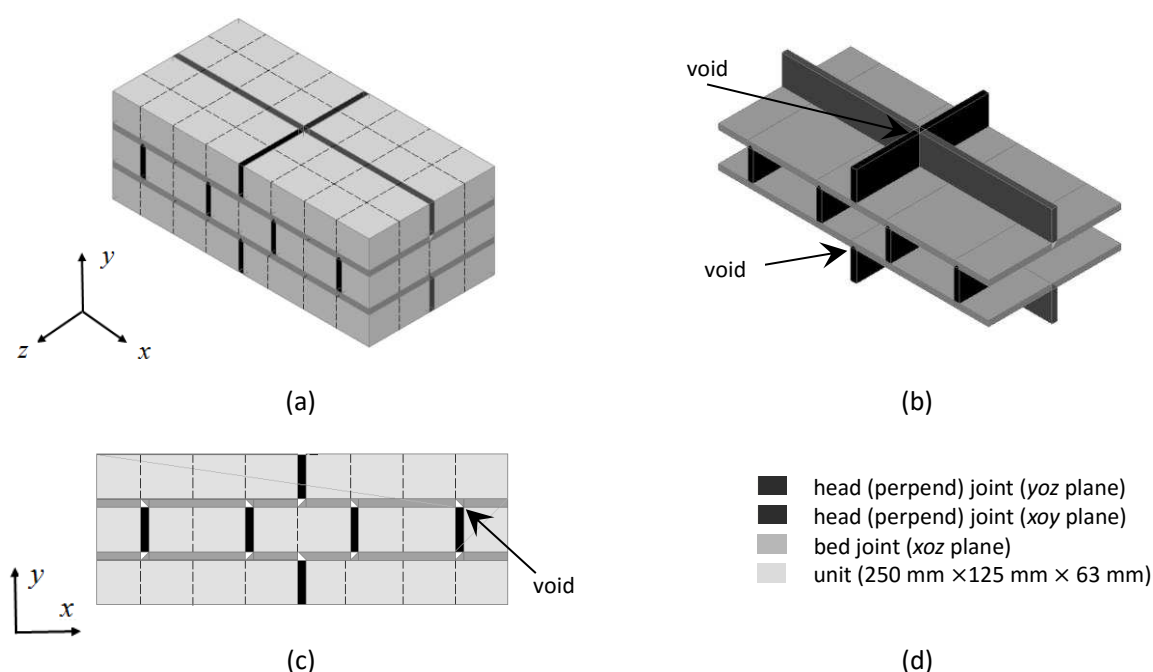### 2.1 Finite element model for unreinforced masonry

122   In the unreinforced masonry model, the bricks and mortar are simulated by two elements: solid

123   elements for groups or "blocks" of masonry units and element-based cohesive elements with zero

124   thickness for the mortar, as shown in Fig.1 (b). The element-based cohesive elements are, hereafter,

125   referred to for convenience as cohesive elements. ABAQUS provides three methods to create

126   cohesive elements. Of these, the authors selected the share node method as it is relatively simple to

127   implement. It should be noted that this method requires the use of cohesive elements with the

128   same mesh density as their surrounding elements. The process to build a multi-leaf masonry model

129   is listed as follows:

130   (1) Create a part of the structure to be modelled with the same geometry as its prototype, in this

131   case an area of multi-leaf masonry construction.

132   (2) Mesh the part referred to above and transfer it to be an orphan part taking care to ensure that

133   the layout of the mortar joints should be representative of the full structure as the subsequently

134   created cohesive elements are based on the initial mesh.

135   (3) Insert the cohesive elements into the region of mortar joints. Take a multi-leaf masonry block

136   where each masonry unit is meshed, for example the blocks shown in Figure 2(a) which are 4 bricks

137   long x 2 bricks wide x 1 brick high. The brick bonding pattern shown is typical of that used in China

138   for multi-leaf brick masonry walls. Each brick is 250mm x 125mm x 63mm in size laid in 10mm thick

139   mortar joints. The thickness of the cohesive elements, exaggerated in Fig.2 for clarity, is zero. The

140   points of intersection of the cohesive elements along different directions were treated as voids

141 (triangular and rectangular voids in Fig.2 (c) and triangular and quadrangular prisms in Fig.2 (b)), to

142 permit co-ordination of the deformation between the cohesive elements and the adjacent solid

143 elements. As the thickness of the cohesive elements is zero, the voids are infinitely small and would,

144 therefore, not have a significant effect on the stiffness of the cohesive elements. It is recommended

145 that the cohesive elements in the *xoz* plane and the *xoy* plane be generated in sequence. The others

146 can then be created in the *yoz* plane, as shown in Fig.2 (b). Alternatively, a subroutine compiled in

147 Matlab can be adopted to generate cohesive elements in all directions at once, as described in Ref.

148 [31].

(a)

(b)

(c)

head (perpend) joint (*yoz* plane)
head (perpend) joint (*xoy* plane)
bed joint (*xoz* plane)
unit (250 mm ×125 mm × 63 mm)

(d)

149 Figure 2. Meso-scale modelling of multi-leaf masonry: (a) multi-leaf masonry sample; (b) mortar

150 joints; (c) side elevation of multi-leaf masonry sample; (d) legend. Note the FE mesh is depicted by

151 dashed lines.

152 **2.2 FRP-reinforced finite element model**

153 The FRP-reinforced masonry model is based on the unreinforced masonry model described in

154 section 2.1. Considering the thickness of FRP is typically around 0.15-0.3 mm, FRP strips are

155 simulated by shell elements. Assuming that there is full bond (or adhesion) between the surface of

156 the masonry and the FRP, the FRP strips in the model are considered to be tied directly to the

157 masonry.

2.3 Constitutive models

2.3.1 Constitutive behaviour of mortar joints

160 Cohesive elements in ABAQUS were developed originally with the aim of modelling adhesives,

161 bonded interfaces, gaskets and rock fracture [32]. Constitutive material models described in

162 ABAQUS are based on a continuum description for adhesives, a traction-separation description for

163 the bonded interfaces, or a uniaxial stress state which is appropriate for modelling gaskets or

164 laterally unconstrained adhesive patches. For different modelling purposes, cohesive elements are

165 assigned with corresponding material constitutive laws. For instance, when the cohesive element

166 represents an adhesive material with a finite thickness, the use of continuum macroscopic

167 properties (such as the modulus of elasticity) is recommended. To reproduce tensile/shear fracture

168 in mortar joints, the behaviour of the zero-thickness cohesive elements is expressed by the

169 relationship of traction versus separation. The traction-separation law is commonly used to simulate

170 sliding or delamination at the interface and can reflect the damage progression of the cohesive

171 element under cyclic loading.

172 The nominal traction stress vector (t) consists of three components: the normal stress vector (t_n)

173 and shear stress vector along s- and t- directions (t_s and t_t), representing normal traction and two

174 shear tractions, respectively. Normal traction is assessed with different rules for tension and

175 compression vectors. With the assumption that the cohesive element is free from damage under

176 pure compression, the compressive traction is assumed to remain elastic throughout the numerical

177 analysis, while the tensile traction, the same as other two shear tractions, is initially defined with

178 linear elastic behaviour, followed by damage evolution behaviour after damage initiation. For

179 clarification purposes it is useful to think of the zero-thickness cohesive element as being composed

180 of two faces, namely the top face and the bottom face. The relative motion of those faces represents

181 the opening or closing of the cohesive element along the thickness direction, expressed by the

182 spatial displacement of cohesive element (δ_n, δ_s and δ_t). The effective displacement δ_m can be

183 defined by [32]:

$$\delta_m = \sqrt{\langle \delta_n \rangle^2 + {\delta_s}^2 + {\delta_t}^2} \tag{2-1}$$

184 where $\langle \ \ \rangle$ is the Macaulay bracket, which is defined as below:

$$\langle x \rangle = \begin{cases} -x, & x < 0 \\ x, & x \geq 0 \end{cases} \tag{2-2}$$

185 It is also necessary to specify the constitutive thickness. It is not appropriate to define an actual

186 thickness of the cohesive element as the constitutive thickness as the use of an infinitesimally small

187 value causes the stiffness per unit length to be infinity. In this paper, the constitutive thickness is set

188 as 1.0 in order to keep the nominal strains equal to the corresponding separations.

189 The traction-separation law involves three criteria in ABAQUS: linear elastic behaviour, a damage

190 initiation criterion and a damage evolution law. Prior to damage initiation, the traction-separation

191 model assumes initially linear elastic behaviour, expressed by equation (2-3) [32]. As coupled

192 behaviour is not considered in this paper, the off-diagonal terms in the elasticity matrix, t, are set to

193 zero.

$$t = \begin{Bmatrix} t_n \\ t_s \\ t_t \end{Bmatrix} = \begin{bmatrix} K_{nn} & K_{ns} & K_{nt} \\ K_{ns} & K_{ss} & K_{st} \\ K_{nt} & K_{st} & K_{tt} \end{bmatrix} \begin{Bmatrix} \varepsilon_n \\ \varepsilon_s \\ \varepsilon_t \end{Bmatrix} = K\varepsilon \tag{2-3}$$

194 The stiffness, K, can be regard as a penalty parameter. Basically, this penalty stiffness should be large

195 enough to avoid penetrations of the adjacent surrounding elements under compression. However, a

196 very large stiffness may result in the ill-conditioning of the elements. It is recommended that the

197 penalty stiffness be calibrated by comparing experiments with simulations [31, 33] or it should be

198 estimated using empirical formulae [34]. The influence of the penalty stiffness on the simulation

199 results is discussed in Section 4.1.

200　Once the stress and/or strains of a material point satisfy the specified damage initiation criteria,

201　degradation is triggered and the subsequent behaviour of the material will be determined by the

202　damage evolution law. The quadratic nominal stress criterion in ABAQUS is adopted as the damage

203　initiation criteria in this paper, while the evolution law is expressed by fracture energy with linear

204　softening. The scalar damage variable, *D*, is introduced to represent damage progression. *D* evolves

205　from 0 at damage initiation and monotonically increases up to D_{max} (≤1), where the elements are

206　considered to be fully damaged. Thus, with proper damage initiation criteria, cohesive elements can

207　be used to reproduce crack initiation and progression in the mortar joints in a masonry assemblage.

208　Even after *D* reaches D_{max} it is important to retain the cohesive elements in the model otherwise

209　ABAQUS will delete the fully damaged elements by default and they will no longer be available to

210　resist any subsequent penetration of the surrounding elements.

211　**2.3.2 Constitutive behaviour of units and FRP**

212　The concrete damage plasticity (CDP) model is selected to simulate the non-linear behaviour of the

213　masonry blocks. This approach can be used to effectively model two typical failure mechanisms,

214　namely tensile fracture and compressive crushing, and also to capture the degradation of the

215　material in cyclic load simulations. The compressive and tensile stress-strain relationships are

216　formulated by equations (2-4) and (2-5). These formulations were originally used for masonry and, in

217　the model described in this paper, are applied for the blocks [21] which are composed of masonry

218　units and mortar joints (as explained in Section 1). The compression constitutive model is deduced

219　from the compression testing of a large number of masonry assemblages [35], while the tensile

220　stress-strain relationship is modified from the design code for concrete and has been verified to be

221　suitable for masonry [36].

$$\frac{\sigma}{f_{cm}} = \frac{h}{1 + (h-1)(\varepsilon/\varepsilon_{cm})^{h/(h-1)}} \frac{\varepsilon}{\varepsilon_{cm}} \qquad (2\text{-}4)$$

$$\begin{cases} \dfrac{\sigma}{f_{tm}} = \left(\dfrac{\varepsilon}{\varepsilon_{tm}}\right) & \varepsilon/\varepsilon_{tm} \leq 1 \\[4mm] \dfrac{\sigma}{f_{tm}} = \left(\dfrac{\varepsilon/\varepsilon_{tm}}{2\left(\varepsilon/\varepsilon_{tm} - 1\right)^{1.7} + \varepsilon/\varepsilon_{tm}}\right) & \varepsilon/\varepsilon_{tm} > 1 \end{cases} \tag{2-5}$$

222   Where f_{cm} and f_{tm} represent the compressive and tensile strength of masonry respectively, ε_{cm} and

223   ε_{tm} are the corresponding strains. The compressive factor, h, is set as 1.633 by default. Damage

224   parameters (d_t, d_c) are calculated from eq. (2-6) which is based on the Energy Equivalence Principle

225   [37]. This equation assumes that the residual elastic energy caused by stress in the damaged

226   material can be evaluated using the same relationship used for the undamaged material.

$$d = 1 - \sqrt{\sigma/E_0 \varepsilon} \tag{2-6}$$

227   where E_0 is the initial stiffness.

228   In the property modulus of ABAQUS, the viscosity parameter is set as 0.001, and the other plasticity

229   factor is set by default. The FRP is assumed to be orthotropic and is characterised by the behaviour

230   of lamina which are assumed to remain elastic. Fracture and delamination failure of the FRP are not

231   considered in this paper.

3. Description of cyclic tests of masonry walls

233   Cyclic load-testing of full-scale brick masonry wall panels reinforced with surface-mounted BFRP

234   strips was carried out in the laboratory at Wuhan University to study the seismic responses of BFRP-

235   reinforced masonry. With identical geometry and materials, the referred specimens are divided into

236   two groups: Group-A with W1 and BW1-1, and Group-B with W2 and BW2-1. The details and

237   configuration of specimens are illustrated in Table 1 and Fig.3. As shown in Fig.3, each specimen

238   consists of three parts: multi-leaf masonry wall, cap beam and base beam. The brick arrangement of

239   the multi-leaf masonry wall is commonly used in China. All the multi-leaf masonry walls were

240   constructed by brick (also called as 'fired common brick' in China) with typical size of 240 mm×115

241   mm×53 mm (L×B×H) and 10mm thickness cement mortar. Both cap beam and base beam are made

of concrete and installed together with multi-leaf masonry part by using epoxy mortar. The epoxy

mortar used has extremely high bond strength so that the horizontal loadings applied on beams

would be transferred to masonry parts effectively. Material properties of masonry unit and mortar

are measured from the material property tests, as listed in Table 1.

The unidirectional basalt fibres were adopted for reinforcement, and the reinforcement schemes are

shown in Fig.3. The BFRP with the width of 300 mm for BW1-1 and 200 mm for BW2-1 was installed

on both side of the wall with cross layout. The horizontally and vertically BFRP strips are attached for

BW1-1 and BW2-1, respectively. The material properties of BFRP were measured according to the

GB/T3354-1999 [38]: density=330 g/m^2; tensile strength=1350 MPa; elastic modulus=96 GPa;

ultimate tensile strain=2.6 %.

Table 1 Details of the test specimens

Specimen		Dimension (mm)	E_m (MPa)	f_{cm} (MPa)	$f_{b,c}$ (MPa)	$f_{m,c}$ (MPa)
Group-A	W1	1500×1000×240	1807	2.46	11.53	5.38
	BW1-1	1500×1000×240	1807	2.46	11.53	5.38
Group-B	W2	1100×1000×240	2400	2.56	11.53	6.23
	BW2-1	1100×1000×240	2400	2.56	11.53	6.23

Note: E_m is the modulus of elasticity of masonry; f_{cm}, $f_{b,c}$ and $f_{m,c}$ are the average compressive strength of masonry, brick

and mortar, respectively.

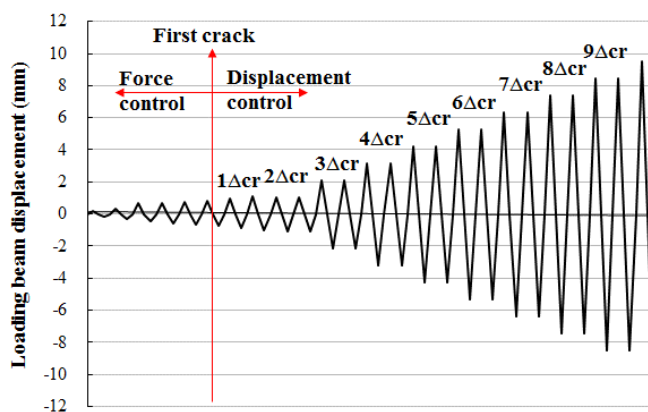
(a)   (b)

(c)

(d)
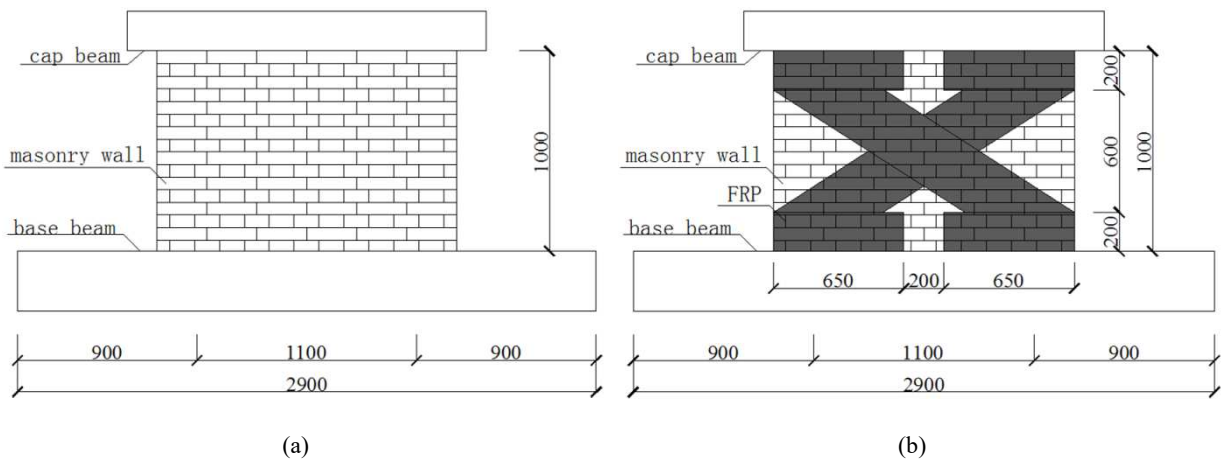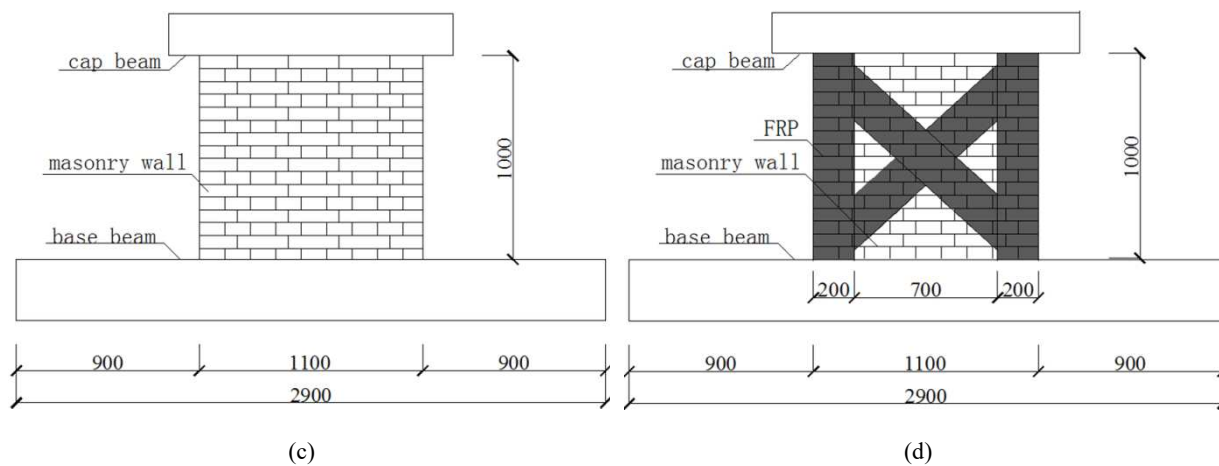
Figure 3.Configurations of specimens: (a) W1; (b) BW1-1; (c) W2; (d) BW1-1.

(a)

(b)

Figure 4. Test procedure: (a) test setup; (b) loading scheme

257 The test setup is shown in Fig.4 (a). The base beam was constrained by four screws in vertical

258 direction and two jacks in lateral direction. In order to keep compressive loadings uniform and

259 vertical, steel rollers were placed between cap beam and transfer beam with equal distances. In

260 addition, rollers were cleaned and polished to eliminate the influence of friction. All specimens were

261 then subjected to a combination of compressive and cyclic lateral loading up to failure. Before the

262 application of the lateral loadings, compressive loadings (namely pre-compression) were firstly

263 applied with value of 0.72 MPa for Group A (W1 and BW1-1) and 1.20 MPa for Group B (W2 and

264 BW2-1), and maintained constantly towards the end of the test. During the test, the cyclic lateral

265 loadings were controlled by force initially and by displacement after cracking occurred. The

266 displacement at cracking initiation is set as Δ_{cr}, and the identical lateral loading scheme for the in-

267 plane cyclic tests is depicted in Fig.4 (b). The test was stopped when the lateral bearing capacity of

268 the specimen declined to 15% of its peak strength, or the specimen was severely damaged and not

269 capable of standing any further load.

4. Validation of the FEM model

271 In this section, the developed numerical models are validated by the aforementioned masonry

272 specimens. Firstly, the influences of numerical parameters, including mesh density and penalty

273 stiffness of cohesive elements, are investigated in Section 4.1, where cyclic and monotonic loading

274 cases are discussed. The unreinforced models (M1 and M2) are constructed with the same geometry,

275 brick arrangement and material properties as the specimens W1 and W2, respectively. Those two

276 models are subjected to monotonic and cyclic loadings in Section 4.2 to assess the shear capacity

277 and aseismic performance of the unreinforced/reinforced masonry walls. Furthermore, according to

278 the BFRP-reinforced specimens (BW1-1 and BW2-1), the BFRP-reinforced models (BM1-1 and BM2-

279 1) are assembled and implemented under monotonic and cyclic loadings in Section 4.2. Similar to

280 Group-A and Group-B, M1 and BM1-1 are grouped as Group-MA, while M2 and BM2-1 are classified

281   as Group-MB. According to the studies in Section 4.1, for Group-MA and Group-MB, each unit are

282   meshed by 4×2×2 (L×B×H); the value of penalty stiffness is set as $5×10^5$ N/mm^3.

283   All the numerical models are simplified into two parts: masonry wall and concrete cap beam. The

284   bottom faces of masonry walls are fixed, while vertical and horizontal loads are applied on concrete

285   cap beam. The compressive pressures of 0.72 MPa and 1.2 MPa, used in cyclic tests, are applied to

286   Group-MA and Group-MB respectively. By referring to the loading process used in the cyclic tests,

287   the compression is firstly loaded which keeps constant in the subsequent simulation, and then the

288   horizontal displacements are introduced on one side of the cap beam. In every numerical model, the

289   horizontal loading mode is the only numerical parameter modified in the monotonic and cyclic

290   simulation. For the monotonic validation, the maximum displacements recorded in tests are loaded

291   for the corresponding numerical models. The tests in Section 3 are mainly focused on the cyclic

292   behaviour of FRP-reinforced and unreinforced masonry walls, the monotonic behaviour of masonry

293   models was verified against existing research achievements as discussed later in Section 4.2.1, *e.g.*

294   the crack patterns agreed well with those reported in [3] and the shear strength of masonry

295   wall agreed with the calculated value using the Chinese Code [39], which has been verified

296   practically to calculate masonry shear strength in [47]. To verify the numerical models under

297   cyclic loadings, the cyclic loading protocols recorded during tests are applied in the corresponding

298   numerical models. In order to save computational resources, the displacement-time loops are only

299   loaded once, rather than twice in tests. This is based on the assumption that the cyclic degradation

300   at the same lateral displacement is minimum, which is validated by the comparison of hysteresis

301   loops from experimental tests and ABAQUS modelling. The cyclic loading protocols for the

302   unreinforced models M1 and M2 are depicted in Fig.5.
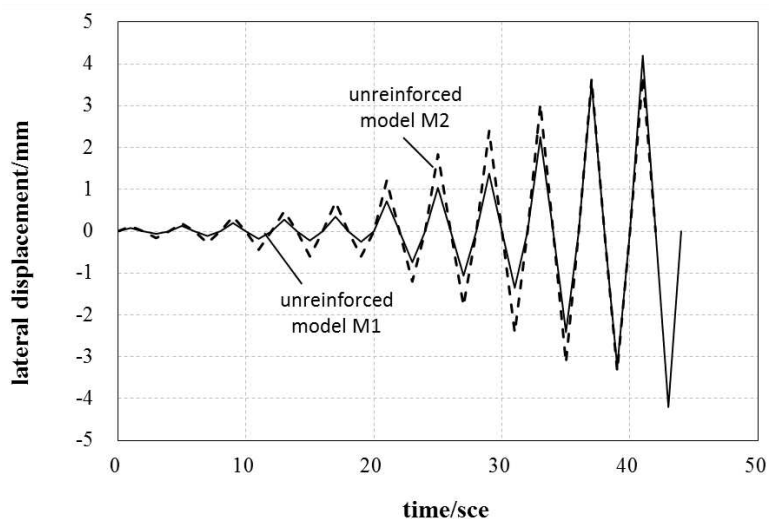
303

304   Figure 5. Cyclic displacement applied on the numerical models.

305   The numerical models under cyclic loadings are validated with the cyclic experimental results, while

306   the modelling results for monotonic loading cases are verified by the related cases in codes

307   (GB50003-2001 [39] and GB50608-2010[40]). It is important to mention that testing procedure plays

308   an significant role on the behaviour of masonry structures [41]. For example, the shear resistance of

309   masonry walls under cyclic loadings is about 10% lower than the one under monotonic loadings [42].

310   Therefore, in terms of monotonic validation, the calculations based on codes are more applicable

311   than the skeleton curves obtained in cyclic tests.

312   Under the assumption that the cap beam does not undergo any damage, it is assigned with an elastic

313   behaviour. The material parameters for masonry units and mortar joints are listed in Table 1 and

314   Table 2. Note that it is hard to obtain the fracture energies of mortar joints in traditional property

315   tests, and different values of fracture energies are used in references (for example, ref. [1], ref. [16]

316   and ref. [19]). Therefore, with reference to those reported values the fracture energies in Table 2

317   were determined by comparing the results of failure strength between standard compressive/shear

318   test specimens and the corresponding numerical models. Mortar joints herein are assumed to be

319   isotropic in the first and second shear directions. Basalt Fibre was measured as 0.1 mm thickness,

320 and after grouted with resin it was combined to become FRP with 0.2 mm thickness. The FRP

321 material parameters are listed in Table 3.

322 Table 2 Material parameters for mortar joints

Material parameter	Group-MA	Group-MB
normal stiffness $E_{n,coh}$/(N/mm^3)	5×10^5	5×10^5
shear stiffness $E_{s,coh}$/(N/mm^3)	5×10^5	5×10^5
normal strength $f_{t,coh}$/MPa	0.13	0.15
shear strength $f_{s,coh}$/MPa	0.75	0.55
Model I fracture energy $G_{f,coh}^{I}$/(mJ/mm^2)	0.09	0.065
Model II fracture energy $G_{f,coh}^{II}$/(mJ/mm^2)	1.126	0.91

323

324 Table 3 Mechanical properties of FRP

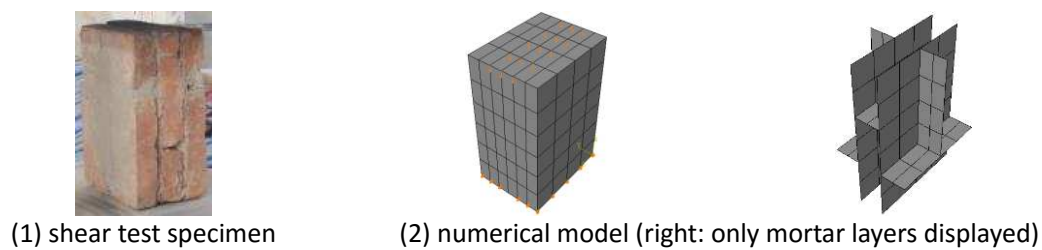| Property	Value	Notes
Longitudinal modulus E_1 (GPa)	96	obtained from property tests
Transverse modulus E_2 (MPa)	8270	obtained from [43]
shear modulus G_{12} (MPa)	5419	obtained from [44]
Major Poisson's ratio v_{12}	0.22	obtained from [45]
Thickness in average t(mm)	0.2	obtained from property tests

325

326 Considering that the penalty stiffness and fracture energies of mortar joints are hard to measure

327 directly, those parameters (in Table1) are determined by comparing the results of

328 compressive/shear masonry strength between standard compression/shear tests and the

329 corresponding ABAQUS models (as shown in Fig.6 and Fig.7, respectively). According to the Chinese

330 Code, those masonry compress/shear standard test specimens were built to detect the

331 compression/shear strength of masonry. As shown in Table 4 and Table 5, those sample ABAQUS

332 models can well reflect the compression and shear strength of the masonry standard

333 compression/shear test specimens.

(1) compression test specimen   (2) numerical model (right: only mortar layers displayed)
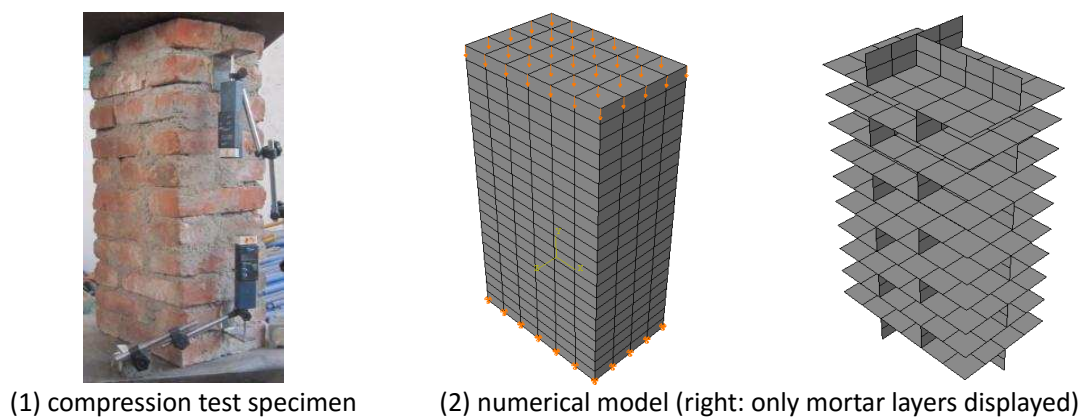
334   Figure 6. Standard compression test of masonry specimens

(1) shear test specimen   (2) numerical model (right: only mortar layers displayed)

335   Figure 7. Standard shear test of masonry specimens

336

337

338   Table 4. Comparison of masonry compressive strength

Masonry specimen	Test results	Numerical results	Difference
Group-A	2.46 MPa	2.55 MPa	3.77%
Group-B	2.56 MPa	2.69 MPa	5.24%

339

340   Table 5. Comparison of masonry shear strength

Masonry specimen	Test results	Test results	Difference
Group-A	0.29 MPs	0.27 MPa	6.23%
Group-B	0.31 MPa	0.34 MPa	8.97%

341

4.1 Convergence study

4.1.1 Influence of mesh density

The unreinforced model M2 is used as a benchmark for mesh sensitivity study. The units are meshed as 4×1×1, 4×2×1, 4×2×2, 8×2×2 and 8×4×2 (L×B×H), respectively. Those models were tested under cyclic and monotonic loadings, and a comparison of simulation results are depicted in Fig.8. Except for the case of 4×1×1 (the coarsest mesh size), the difference between cases is not significant and mainly occurred at the last loading cycle. It is illustrated that the numerical model in this paper is less sensitive when the mesh density along the width is larger than two. In order to save computer resource while still maintain the accuracy of the model, the mesh size (4×2×2) is adopted.

(a)   (b)
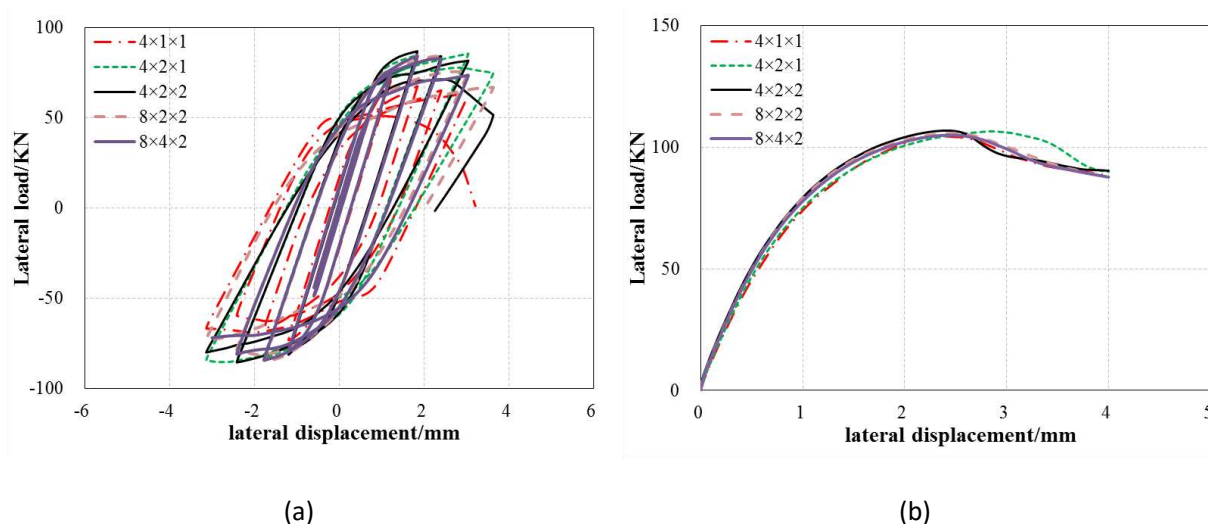
Figure 8. Influence of mesh density in the unreinforced numerical model: (a) cyclic; (b) monotonic.

4.1.2 Influence of penalty stiffness

As referred in Section 2.3.1, the influence of penalty stiffness on cohesive elements was assessed. Take the unreinforced model M2 and the BFRP-unreinforced model MB2-1 as example and set the meshed size as 4×2×2 for each unit. The interface stiffness was factored by 0.1, 0.05 and 10 (i.e. $5×10^4$ N/mm^3, $2.5×10^4$ N/mm^3 and $5×10^6$ N/mm^3), with the reference value of $5×10^5$ N/mm^3 (factor is 1.0). The simulation results are compared in Fig.9 and Fig.10.

358   Except for the case of the smallest penalty stiffness ($2.5×10^4$ N/mm^3) under cyclic loadings, the

359   unreinforced model is almost insensitive to penalty stiffness under cyclic and monotonic loadings, as

360   shown in Fig.9. In Fig.10, for the BFRP-reinforced model, the influence of penalty stiffness is

361   negligible in cyclic case and is small in the monotonic case. Overall, penalty stiffness does not play a

362   significant role on both unreinforced and FRP-reinforced numerical models when models are under

363   cyclic and monotonic loadings. Only the smallest penalty stiffness causes the deterioration of

364   cohesive elements and a sudden loss of strength, so the value of penalty stiffness is recommended

365   to be larger than $2.5×10^4$ N/mm^3. Accordingly, $5×10^5$ N/mm^3 is used for penalty stiffness.

(a)   (b)
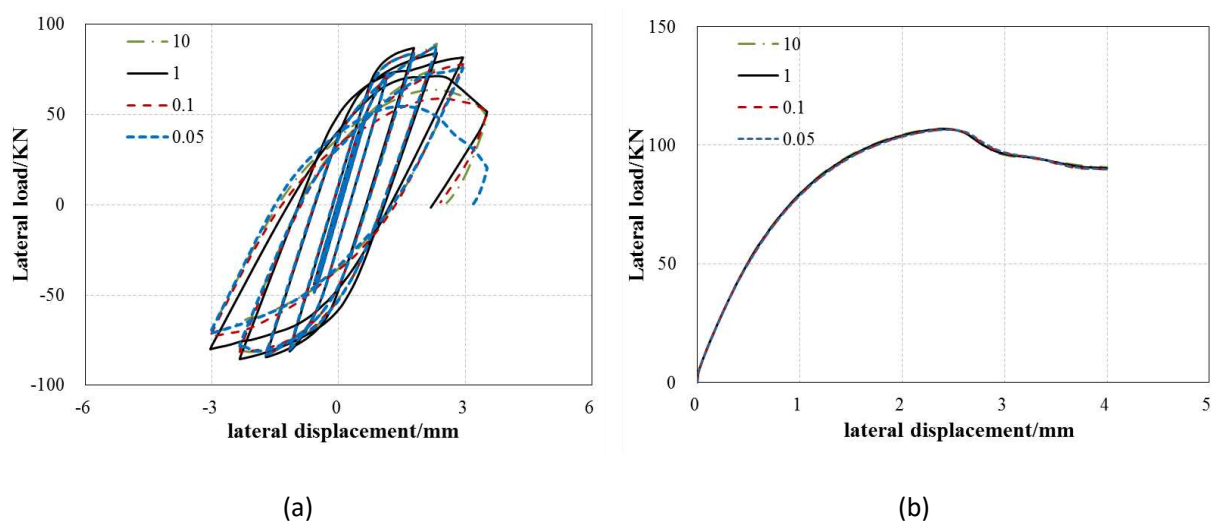
366   Figure 9. Influence of penalty stiffness for the unreinforced numerical model: (a) cyclic; (b)

367   monotonic
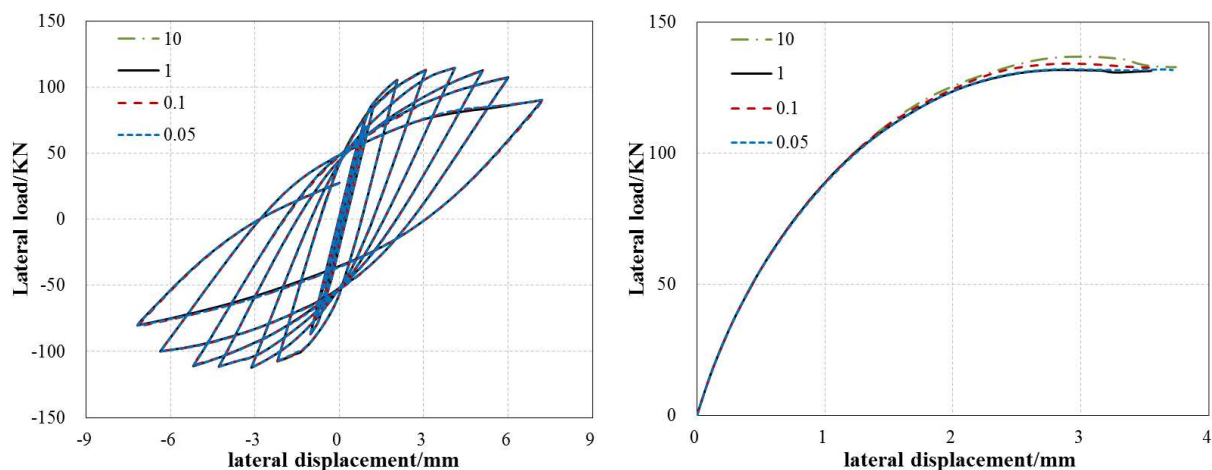
(a)   (b)

368   Figure 10. Influence of penalty stiffness in the BFRP-reinforced numerical model: (a) cyclic; (b)

369   monotonic.

4.2 Unreinforced FEM model

370

4.2.1 Monotonic loading

371

372   According to GB50003-2001[39], the shear strength of unreinforced masonry V_0 is calculated by:

$$V_0 = (f_v + \alpha\mu\sigma_0)A \qquad\qquad (4\text{-}1)$$

373   where the design value of shear strength for masonry (f_v), the modified coefficient (α) and the

374   influence coefficient under shear-compression load (μ) are determined by GB50003-2001[39]; σ_0 is

375   the compressive loading, which equal to 0.72 MPa for Group-A and 1.2 MPa for Group-B; A is the

376   cross sectional area of a masonry wall.

377   Table 6 Calculated results for monotonic loading

Specimen	f_v (MPa)	$\alpha\mu$	$\alpha_2\mu_2$	η	V_0(KN)	$V_{u,m}$ (KN)	$V_{u,f}$ (KN)	V_u (KN)
W1	0.29	0.13	--		138.0	--	--	--
BW1-1	0.29	0.13	0.195	1.36	138.0	155.75	43.93	199.68
W2	0.312	0.11	--		117.2	--	--	--
BW2-1	0.312	0.11	0.187	1.38	117.2	143.93	8.56	152.49

378   The calculated and numerical results are shown in Table 6 and Fig.11, respectively. A good

379   agreement between the calculated and simulation results can be observed, in terms of the shear

380   strength. The shear strength of M1 is only 0.57% larger than that of W1; the error between M2 and

381   W2 is 8.87%. in Fig.11, The colour of mortar layers are ranged from white to black, to represent

382   damage evolution from intact to overall damaged degrees. It is found the crack patterns in

383   numerical models are mainly caused by shear failure, similar to cracks observed in monotonic tests

384   [3, 26]. Therefore, the unreinforced FEM models can accurately assess the peak strength of the

385 unreinforced masonry walls, and cracking patterns are successfully captured to reflect the

386 monotonic behaviour of the unreinforced masonry walls.

387

(a)   (b)
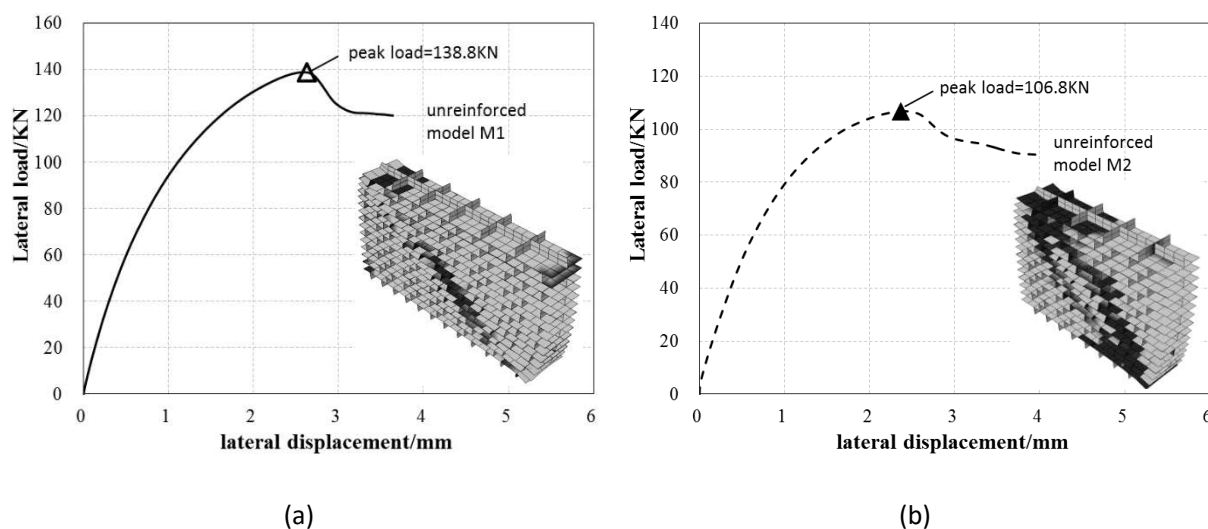
388   Figure 11. Numerical results of unreinforced masonry walls under monotonic loading:

389   (a) M1; (b) M2; (insert) cracking patterns.

390 **4.2.2 Cyclic loading**

391 In this section, the numerical results from the unreinforced model under cyclic loadings are verified

392 by the experimental results, in terms of hysteresis loop, degradation of stiffness and cracking

393 pattern. For the specimen W2, the experimental results, marked as ABC curve in Fig.12(b), are

394 regarded as invalid. Because at that time, the specimen was severely damaged with large

395 deformation, causing the reading of several LVDTs deviated to the extent that they are deemed as

396 unreliable. Comparisons of the hysteresis loop between the experimental and numerical results are

397 illustrated in Fig.12. A good agreement among hysteresis loop between the results of experiments

398 and simulation can be observed. And the trend of stiffness degradation is similar between

399 experimental and simulation results. For specimens W1 and W2, the loss of strength was relatively

400 more significant than that of the numerical models (M1 and M2) after the peak strength is reached.

401   For the specimen W2, the positive peak strength and its corresponding displacement are

402   distinctively different from the negative ones, as shown in Fig.12 (b). It indicates that even for one

403   single wall, the mechanical properties of its two sides are not the same. The deviation is primarily

404   caused by the heterogeneity of masonry materials and possibly workmanship as well. That is one of

405   the reasons that the positive peak strength of the specimen W2 occurred much later than that of the

406   model M2, but the negative peak strength of W2 and M2 were achieved at the same displacement.

407   Another reason is the internal damage caused by hoisting and instalment of specimens during the
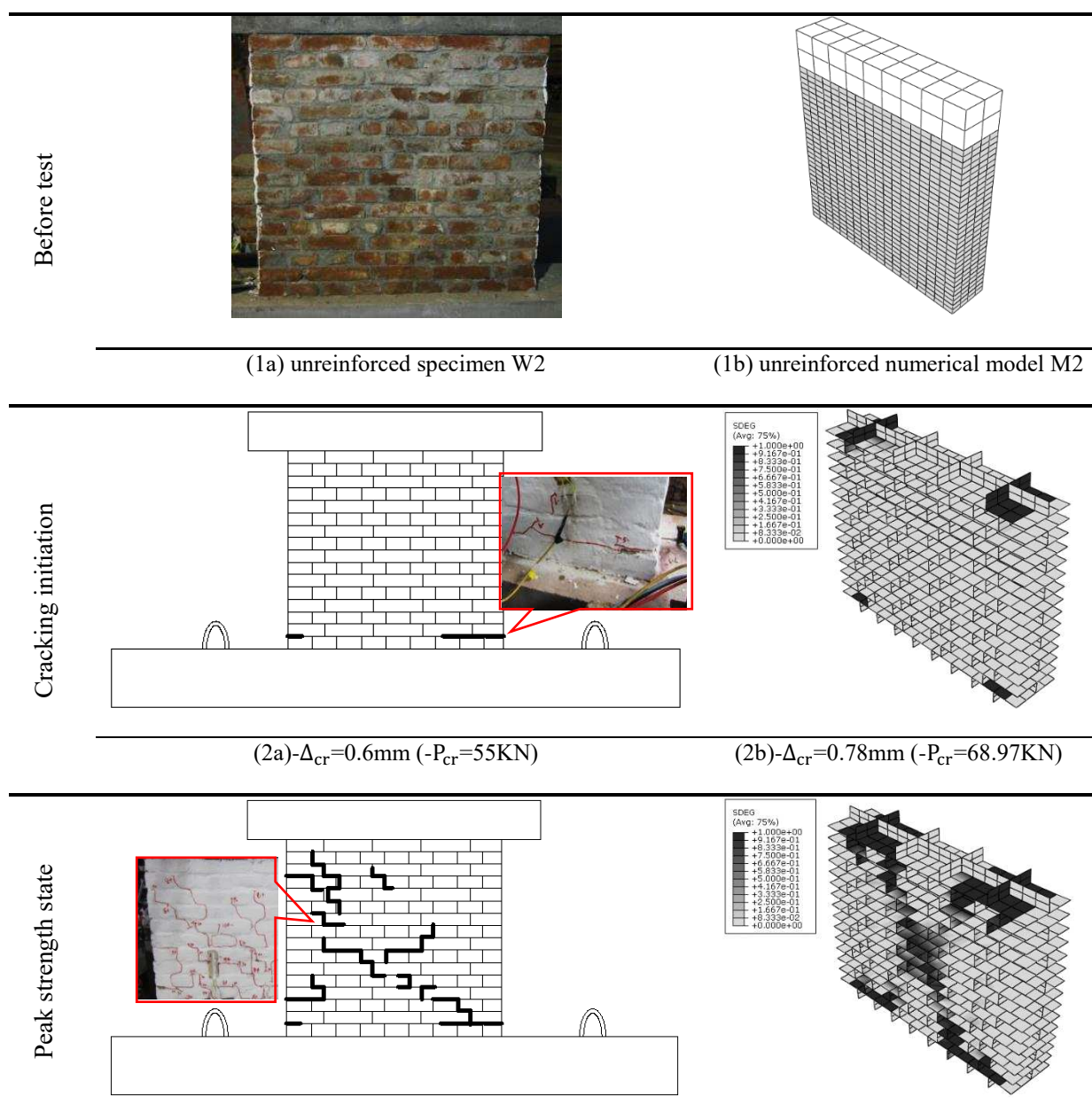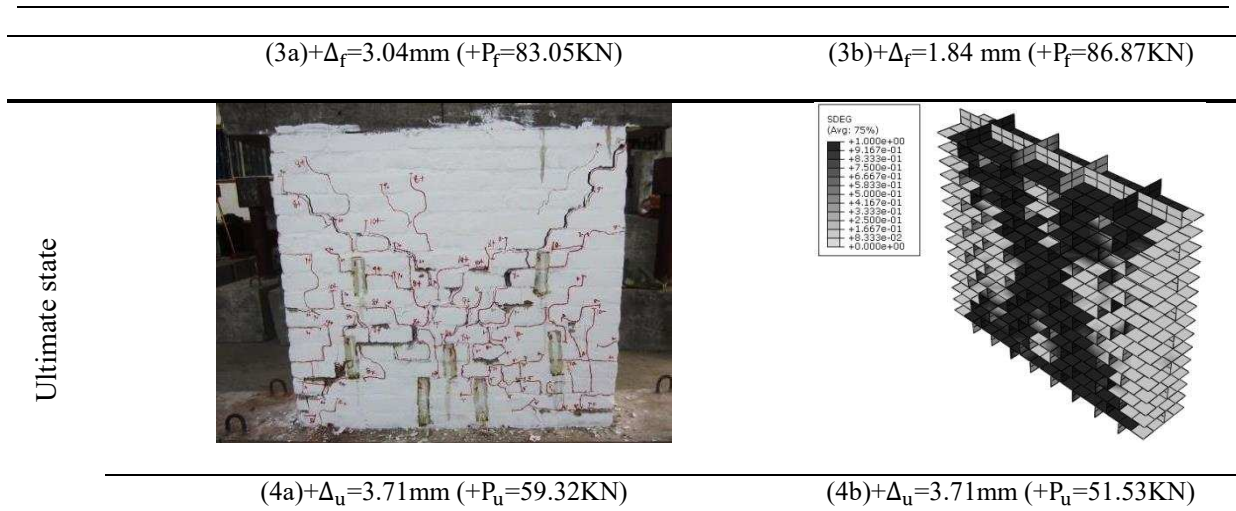
408   preparation stage.

(a)   (b)
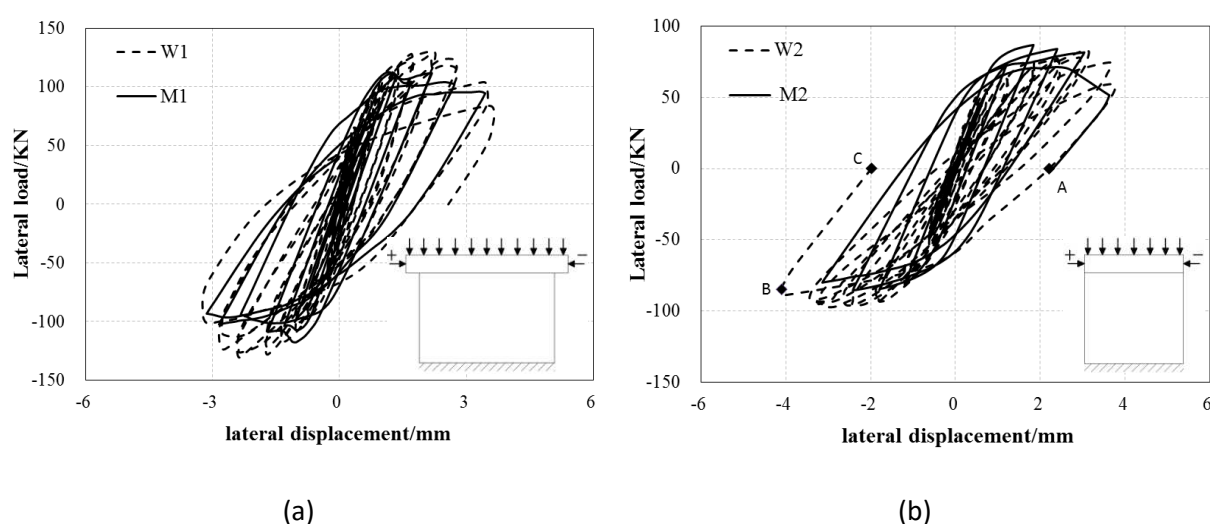
409   Figure 12.Comparison of hysteresis loop: (a) W1 and M1; (b) W2 and M2; (insert) definition of

410   loading direction, "+" is the positive loading direction and "−" is the negative loading direction.

411   To investigate the cracking progression, the cracking patterns of W2 and M2 at the key loading

412   stages are listed in Table 7. The left column (Table7 (1a)–(4a)) depicts the cracks on the specimen

413   W2, while the right column (Table7 (1b)-(4b)) presents the simulation results of M2. For the

414   specimen W2, the initial cracks were detected at the corners of the masonry wall when the lateral

415   loading of 55KN was loaded (as shown in Table 7 (2a)). Afterwards, cracks progressed from the

416   corners towards the centre, forming a diagonal cracking pattern. The specimen failed with

417   brittleness after reaching the peak strength at 3.04mm displacement. At ultimate displacement of

3.71 mm, W2 fractured into four pieces and the maximum crack was up to 1-2 cm in width, as shown

in Table 7 (4a). In the case of the numerical model M2, cracks initiate from corners and continued to

develop to a diagonal pattern. Similar to experimental records, the diagonal cracks in numerical

model extend in width during the cyclic loading, as shown in Table 7(4a)-(4b). Therefore, the

unreinforced models proposed in this paper can accurately reflect the cyclic responses of the

unreinforced masonry walls.

Table 7 Cracking pattern of unreinforced masonry

| Before test | (1a) unreinforced specimen W2 | (1b) unreinforced numerical model M2 |

Cracking initiation

(2a)-Δ_{cr}=0.6mm (-P_{cr}=55KN)   (2b)-Δ_{cr}=0.78mm (-P_{cr}=68.97KN)

Peak strength state

(3a)+Δ_f=3.04mm (+P_f=83.05KN)	(3b)+Δ_f=1.84 mm (+P_f=86.87KN)

Ultimate state

(4a)+Δ_u=3.71mm (+P_u=59.32KN)	(4b)+Δ_u=3.71mm (+P_u=51.53KN)

425 Note: Δ_{cr}, Δ_f and Δ_u are the displacement at cracking initiation, peak state and ultimate limit state; P_{cr}, P_f and P_u are their

426 corresponding strength.

4.3 BFRP-reinforced FEM model

4.3.1 Monotonic loading

429 According to the Eurocode for masonry [46] and the Chinese code (GB50608-2010) [40], the shear

430 capacity of the FRP-reinforced masonry is the sum of two parts, *i.e.*, the shear capacity of the

431 unreinforced masonry wall ($V_{u,m}$) plus the additional capacity provided directly by the FRP

432 reinforcement ($V_{u,f}$):

$$V_u = V_{u,m} + V_{u,f} \tag{4-2}$$

433

434 As a result of the interaction between the FRP strips and the masonry, $V_{u,m}$ is larger than the peak

435 strength of the corresponding unreinforced masonry wall (V_0). According to the Chinese code

436 [40], $V_{u,m}$ herein is calculated by equation (4-3). The increase caused by the FRP-masonry interaction

437 is basically expressed by the value of the modified coefficient and the influence coefficient under

438 shear-compression load for the reinforced masonry walls (α_2 and μ_2) and the influence coefficient of

439 reinforcement η.

$$V_{u,m} = (f_v + \eta\alpha_2\mu_2\sigma_0)A \tag{4-3}$$

440

441   To date a number of codes define the formulae to obtain the contribution of FRP reinforcement. Eq.

442   (4-4) from the Chinese standard [40] is adopted to assess $V_{u,f}$. Although studies [47] show that that

443   the Chinese standard has a relatively higher deviation, it is a developed code that takes the

444   reinforcement scheme into consideration.

$$V_{u,f} = \zeta E_f \varepsilon_{fd} \sum_{i=1}^{n} A_{fi} \cos \theta_i \qquad (4\text{-}4)$$

445

446   where ζ is the efficient coefficient of FRP reinforcement, set as 1.0 for the single cross layout [40]. E_f

447   and ε_{fd} represents the elastic modulus and effective strain of FRP strips (equals to $\varepsilon_{fe}/\gamma_e$). ε_{fe} is the

448   effective strain of FRP strips. Due to that the kind of FRP material do not have significant influence

449   on the improvement of peak strength [47], ε_{fe} can be a fixed value, with 0.001 for unanchored FRP

450   strips and 0.0015 for anchored FRP strips [40]. γ_e accounts for the environmental influence; for the

451   BFRP reinforcement indoor, γ_e=1. A_{fi} account for the cross section area of masonry and FRP strips.

452   The angle between the FRP reinforcement and courses, θ, is 35^0 for BW1-1 and 42^0 for BW2-1. This

453   confirms what has been reported in previous studies that different configurations of FRP

454   reinforcement lead to different increase rates of masonry shear strength [3, 48]. Apart from the

455   shear capacity obtained from cross reinforcement, the horizontal FRP strips can obviously enhance

456   the shear capacity of masonry walls under monotonic loading, while far less contribution to the

457   shear capacity is assumed for the vertical FRP strips without anchors [3]. Therefore, in this case, $V_{u,f}$

458   is the sum of the cross and horizontal reinforcement, as listed in Table 6.

459   The numerical results,V_c, are 227.87KN for BM2-1 and 134.12KN for BM2-2. The corresponding ratio

460   of calculated and numerical results is 1.14 and 0.88, respectively. It indicates that the FRP-reinforced

461   models are almost in accordance with the Chinese code within an acceptable deviation. Considering

462   that many factors influence the accuracy of code calculation [47], the FRP-reinforced models in this

463   paper can effectively assess the peak strength of the FRP reinforced masonry walls under monotonic

464   loadings.

4.3.2 Cyclic loading

466   The load-displacement envelope curves obtained by experiment and simulation are presented in

467   Fig.13. It can be observed that the simulation and experimental results have a good agreement with

468   each other. Fig.14 illustrates a similarity in cracking patterns between the BFRP-reinforced specimen

469   BW2-1 and numerical model BM2-1. Meanwhile, similar shear cracks are observed for the specimen

470   BW2-1 and the model BM2-1 within the unreinforced areas (Table 8 (4a) and (4b)), indicating that

471   the developed numerical models for BFRP-reinforced masonry can effectively reproduce the damage

472   progression in the FRP-reinforced masonry walls.

473   For the experiment studies on the FRP-reinforced masonry, the cracks under FRP strips are very

474   difficult to detect and monitor precisely. This drawback can be overcome by the FRP-reinforced

475   numerical model. The cracks underneath FRP in BM2-2 are presented from Table 8 (2b) to Table 8

476   (4b), where the damage progression under BFRP reinforcements is clearly captured. As shown in

477   Table 8 (2a)-(2b), the initial cracks in BW2-1 are accurately reproduced in BM2-1, but more cracks

478   emerge at the upper reinforced parts which are the undetected area in experiments. Furthermore,

479   by removing the FRP strips in the display of the modelling results, the cracking pattern under FRP

480   reinforcement can be revealed. Overall, the FRP-reinforced models can successfully reflect the

481   seismic behaviour and the cracking progression of the FRP-reinforced masonry walls.

(a) (b)
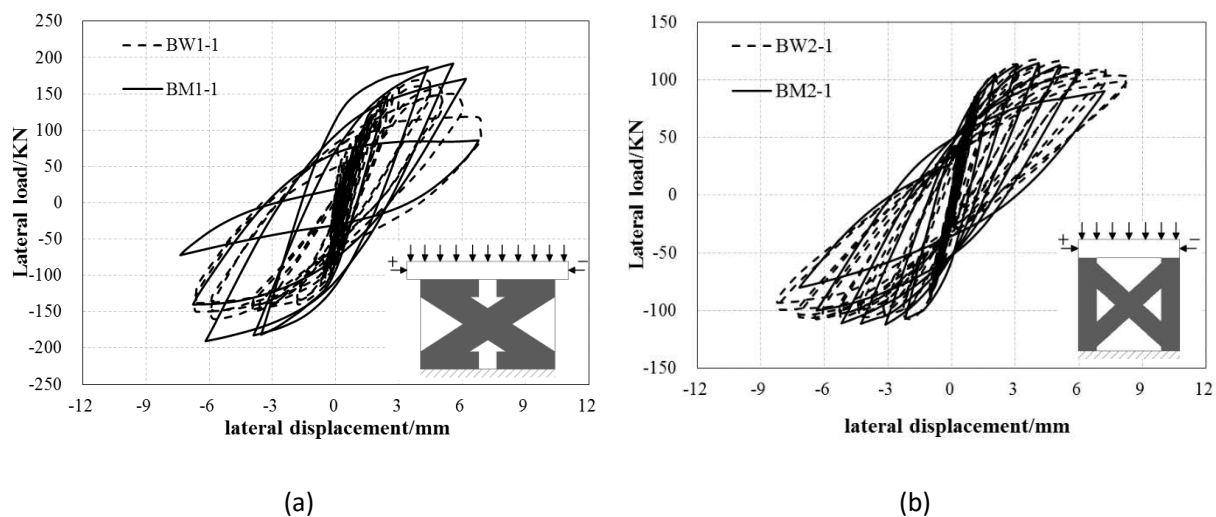
Figure 13. Hysteresis loop of BFRP-reinforced masonry: (a) W1 and M1; (b) W2 and M2; (insert) definition of loading direction, "+" is the positive loading direction and "−" is the negative loading direction.

(a) (b)
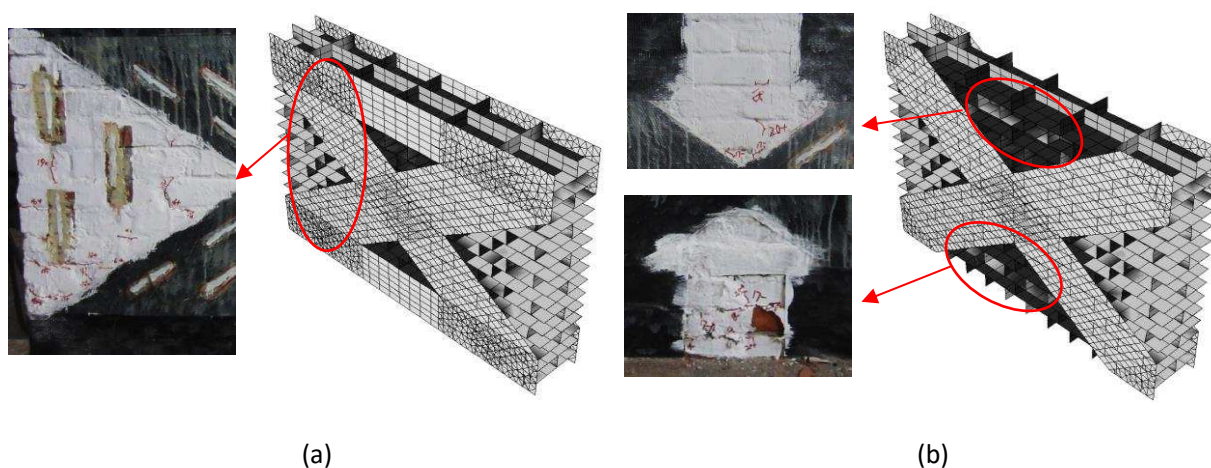
Figure 14. Cracking pattern of the BFRP-reinforced masonry (BW1-1 and BM1-1): (a) displayed with horizontal reinforcement; (b) displayed without horizontal reinforcement; (insert) zoomed-in images from experiments at corresponding positions for comparisons.
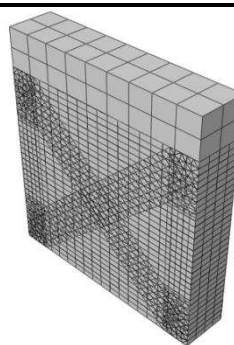
Table 8 Cracking pattern of the BFRP-reinforced masonry walls (BW2-1 and BM2-1)

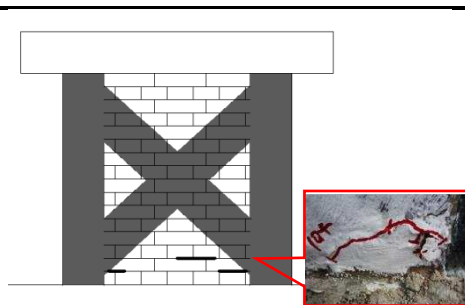(1a) BFRP-reinforced specimen BW2-1   (1b) BFRP-reinforced numerical model BM2-1
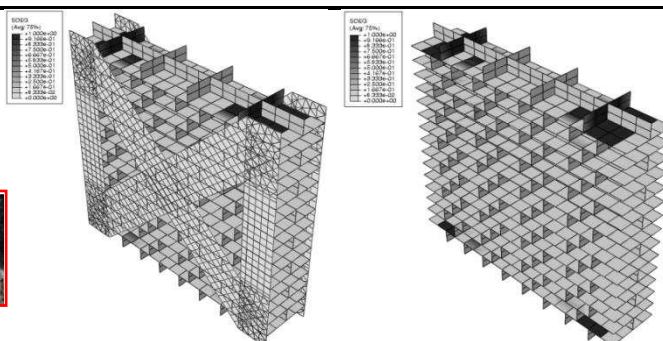
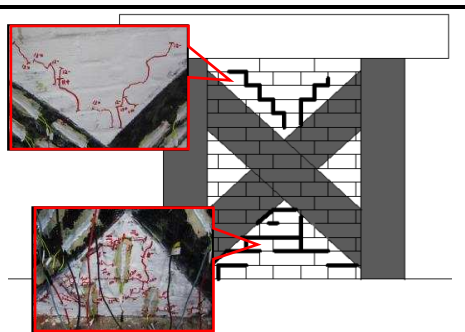(2a) $-\Delta_{cr}$=1.06mm($-P_{cr}$=90.17KN)   (2b) $-\Delta_{cr}$=1.06mm($-P_{cr}$=86.76KN)

(3a) $+\Delta_f$=4.23mm($+P_f$=117.63KN)   (3b) $+\Delta_f$=4.23mm($+P_f$=114.54KN)
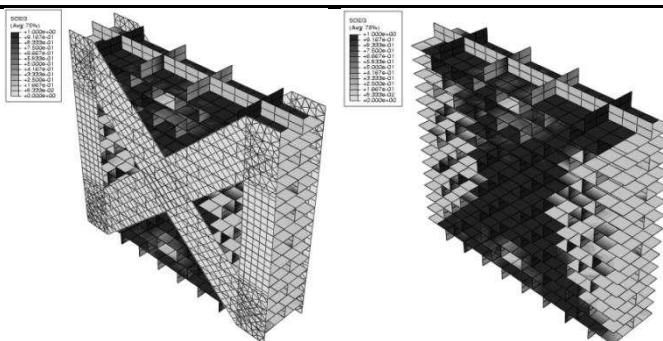
(4a) $+\Delta_u$=8.53mm($+P_u$=98.81KN)   (4b) $+\Delta_u$=7.43 ($+P_u$=90.24KN)

Before test

Cracking initiation

Peak strength state
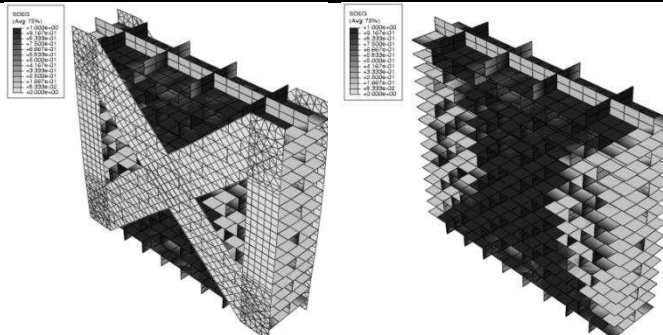
Ultimate state

490

491   For the diagonal FRP strips in BM2-1, the contour of the maximum principal stress is depicted at peak

492   strength and ultimate states (shown in Figure 15). According to Figure 15, when the reinforced

493   masonry wall reaches its peak strength state and ultimate state, the maximum stresses of the

494   diagonal FRP strips are approximately equal to 344 MPa and 378 MPa, respectively, which are both

495   far less than the typical tensile failure strength of BFRP. The finite element simulations also show that

496   the maximum stress of FRP strips increase progressively during the last few circles and the FRP strips

497   still work without failure.

(1) Peak strength state   (2) Ultimate state
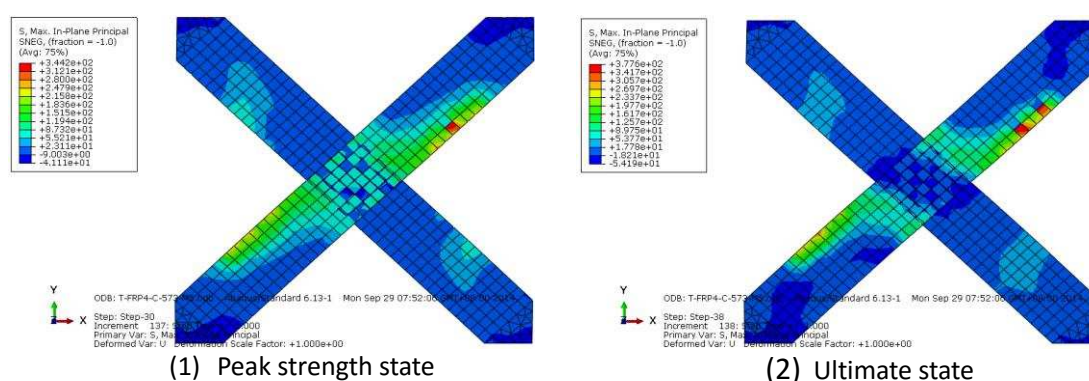
498   Figure 15. Maximum principal stresses in FRP

499

4.4 Assessment of FRP reinforcement

501   Since the late 1990s, a large number of experimental studies have been carried out to assess the

502   effectiveness of reinforcement [1-3]. With the help of numerical analysis, the reinforcing

503   effectiveness can be assessed or predicted in a general and economic way. In this section, the effects

504   of FRP reinforcement on masonry are analysed.

505   Table 9 illustrates a comparison between the ductility factors obtained from experiments and

506   simulations. The ductility factors are calculated according to Ref. [41]. Compared with the

507   unreinforced specimen W2 and numerical model M2, the ductility and resistance to cyclic load are

508   greatly improved for the BFRP-reinforced specimens BW2-1 and numerical models BM2-1 with

509   similar amplitude. It indicates that the FRP reinforcement with cross layout and vertical anchors can

510   effectively enhance the ductility of masonry walls and the numerical model can capture the

511 development of ductility accurately. As shown in Table 9, the horizontal anchors have minimal

512 influence on the ductility capacity, although the FRP reinforcement with cross layout is adopted for

513 masonry walls. It is worth noting that the horizontal FRP anchored at the base of the masonry wall

514 causes high compressive stresses at the base corner. This indicates that the horizontal strips are hard

515 to slow down the shear-sliding effectively, which shows good agreement with the conclusions in Ref.

516 [49]. For the specimen BW1-1, the high compressive stresses causes the brittle fracture at ultimate,

517 including brick crushing at the corners and the de-bonding between BFRP and masonry. However,

518 the de-bonding behaviour is assumed to be neglected during simulations. That may be the reason

519 why, the development of ductility for the specimen BW1-1 is less than the numerical model BM1-1.

520 Table 9 ductility factors for the experiment specimens and numerical models

Specimen		P_f (KN)	H_u (KN)	d_e (mm)	d_u (mm)	μ_u	Δ (%)
Experiment							
Group-A	W1	130.34	117.31	0.28	3.5	12.68	
	BW1-1	168.14	151.33	0.49	6.7	13.75	8.42
Group-B	W2	83.05	74.75	0.52	3.71	7.12	
	BW2-1	117.63	105.87	0.71	8.53	11.99	68.32
Simulation							
Group-MA	M1	111.55	100.39	1.06	3.5	3.32	
	BM1-1	191.48	172.332	1.656	6.7	4.045	21.95
Group-MB	M2	86.87	78.19	1.05	3.71	3.54	
	BM2-1	114.54	103.09	1.31	7.43	5.66	59.96

521 Note: d_e is the displacement at the idealised elastic limit; d_u is the maximum displacement for the idealised force-

522 displacement relationship for masonry; μ_u is the ductility factor; Δ is the improvement between unreinforced and

523 reinforced masonry walls.

524 For the unreinforced specimen W2, the cracking pattern was typically diagonal, while the shear

525 cracks in the BFRP-reinforced specimen BW2-1 were found in every unreinforced part. Besides, the

526   lower part of BW2-1 was seriously damaged, but almost no crack was recorded at that part of W2.

527   The experimental observation illustrates that the FRP reinforcement develops the attribution of

528   cracks much more evenly, indicating that the BFRP reinforcement brings changes in the cracking

529   pattern. Similar changes in cracking pattern are also observed in the numerical results of the

530   unreinforced and FRP-reinforced models, M2 and BM2-1, (Table 7 and Table 8). In addition, in Table

531   8(4b), the BM2-1 has a wider diagonal cracking pattern than M2 and additional shear cracks are

532   observed in the unreinforced zones. Therefore, the developed models can reflect and assess the

533   effectiveness of FRP reinforcement on the masonry walls before and after reinforcement in terms of

534   cracking pattern.

5. Conclusions

536   This paper describes a new development in modelling the behaviour of the unreinforced and FRP-

537   reinforced masonry walls under monotonic and cyclic loading conditions. In the developed meso-

538   scale models, the element-based cohesive element is adopted to simulate mortar joints. Simulations

539   were conducted to evaluate the accuracy and effectiveness of the developed models under both

540   monotonic and cyclic loadings. The numerical results are analysed and compared with code and

541   experimental results. The conclusions are summarised as following:

542   (1) The unreinforced masonry specimens are effectively simulated by the developed models.

543   The cracking initiation takes place at the same time and positions; the similar diagonal

544   cracking pattern is also observed. Compared with experimental observations, the cracks in

545   simulation results are relatively wider and evenly distributed.

546   (2) The FRP-reinforced masonry models also produced similar cracking patterns observed in the

547   FRP-reinforced masonry experiments. Besides, the cracks under reinforcement can be clearly

548   displayed by removing the reinforcement in the display of the simulation results, but cannot

549   be observed directly in the lab tests. The developed models can provide more insights of the

550   behaviour of FRP-reinforced masonry walls than experimental studies.

551   (3) Under cyclic loadings, the seismic behaviours of the masonry before and after reinforcement

552   are effectively simulated by the developed models. Comparison between the experimental

553   and numerical results shows a close agreement of stiffness degradation and peak strength.

554   Based on the related codes, the calculated results of masonry walls are adopted to validate

555   the monotonic simulation. The simulations match the calculated results accurately.

556   (4) The unreinforced masonry models successfully capture the feature of brittleness for the

557   unreinforced masonry walls. After installing with FRP strips, the reinforced masonry models

558   improve the ductility as well as the seismic resistance of the wall. By comparing with the

559   experimental results, the numerical simulation is verified to have the capacity to assess the

560   effect of FRP reinforcement. Therefore, the developed models are applicable to predict the

561   reinforcement effects.

562   (5) With the built-in constitutive material model in ABAQUS, the element-based cohesive

563   element can effectively reflect the damage progression and the nonlinear behaviour of at

564   mortar joints.

565   (6) The convergence studies on mesh density and penalty stiffness indicate that the proposed

566   models are moderately sensitive under monotonic and cyclic loadings. Thus, the numerical

567   models with cohesive elements are able to overcome the convergence and stability problem.

568

569   Although the developed models have been proved to be efficient and accurate for the cases

570   studied, more work still needs to be carried out for improvement. A perfect adhesion

571   between FRP and masonry was assumed in the current model, and as a result a significant

572   loss of strength after reaching the peak value is observed in the simulations of FRP reinforced

573   cases. Thus, the fracture caused by de-bonding and slipping between FRP and masonry need

574   to be considered in future models. Another improvement can be made by considering the

575   cracks within bricks.

580 References

581 [1] Triantafillou TC. Strengthening of masonry structures using epoxy-bonded FRP laminates. Journal

582 of composites for construction. 1998;2(2):96-104.

583 [2] Nanni A, Tumialan JG. Fiber-reinforced composites for the strengthening of masonry structures.

584 Structural engineering international. 2003;13(4):271-8.

585 [3] Marcari G, Manfredi G, Prota A, Pecce M. In-plane shear performance of masonry panels

586 strengthened with FRP. Composites Part B: Engineering. 2007;38(7–8):887-901.

587 [4] Xu L, Zhang S, Hu X, Zhang M. Seismic Responses of Masonry Structures Strengthened with FRP

588 Laminates: a Shaking-table Study. 15 WCEE Proceedings. Lisboa. 2012.

589 [5] Zhou D, Lei Z, Wang J. In-plane behavior of seismically damaged masonry walls repaired with

590 external BFRP. Composite Structures. 2013;102:9-19.

591 [6] Alcaino P, Santa-Maria H. Experimental response of externally retrofitted masonry walls

592 subjected to shear loading. Journal of Composites for Construction. 2008;12(5):489-98.

593 [7] Mandara A, Scognamiglio D. Prediction of collapse behavior of confined masonry members with

594 ABAQUS. Proc of the ABAQUS Users' Conference, Munich2003.

595 [8] Karapitta L, Mouzakis H, Carydis P. Explicit finite‐element analysis for the in‐plane cyclic

596 behavior of unreinforced masonry structures. Earthquake Engineering & Structural Dynamics.

597 2011;40(2):175-93.

598 [9] Dhanasekar M, Haider W. Explicit finite element analysis of lightly reinforced masonry shear walls.

599 Computers & Structures. 2008;86(1–2):15-26.

600   [10] Agnihotri P, Singhal V, Rai DC. Effect of in-plane damage on out-of-plane strength of

601   unreinforced masonry walls. Engineering Structures. 2013;57:1-11.

602   [11] Giordano A, Mele E, De Luca A. Modelling of historical masonry structures: comparison of

603   different approaches through a case study. Engineering Structures. 2002;24(8):1057-69.

604   [12] Prakash SS, Alagusundaramoorthy P. Load resistance of masonry wallettes and shear triplets

605   retrofitted with GFRP composites. Cement and Concrete Composites. 2008;30(8):745-61.

606   [13] Zucchini A, Lourenço PB. A coupled homogenisation–damage model for masonry cracking.

607   Computers & Structures. 2004;82(11–12):917-29.

608   [14] Zucchini A, Lourenço PB. Mechanics of masonry in compression: Results from a homogenisation

609   approach. Computers & structures. 2007;85(3):193-204.

610   [15] Zucchini A, Lourenço PB. A micro-mechanical homogenisation model for masonry: Application

611   to shear walls. International Journal of Solids and Structures. 2009;46(3–4):871-86.

612   [16] Rekik A, Lebon F. Homogenization methods for interface modeling in damaged masonry.

613   Advances in Engineering Software. 2012;46(1):35-42.

614   [17] Burnett S, Gilbert M, Molyneaux T, Beattie G, Hobbs B. The performance of unreinforced

615   masonry walls subjected to low-velocity impacts: Finite element analysis. International Journal of

616   Impact Engineering. 2007;34(8):1433-50.

617   [18] Milani G. 3D upper bound limit analysis of multi-leaf masonry walls. International Journal of

618   Mechanical Sciences. 2008;50(4):817-36.

619   [19] Xiong G. Experimental researches and finite element analysis on brick masonry strengthened

620   with GFRP [D]. Changsha: Changsha University of Science & Technology; 2012. (in Chinese)

621   [20] Łodygowski T, Sielicki PW. The behavior of masonry walls subjected to unusual dynamic loading.

622   Computer Methods in Mechanics, Zielona Góra, Poland 2009.

623   [21] Kong J, Zhai C, Li S, Xie L. Study on in-plane seismic performance of solid masonry-infilled RC

624   frames. China Civil Engineering Journal. 2012;45(supple 2):137-41. (in Chinese)

625 [22] Aref AJ, Dolatshahi KM. A three-dimensional cyclic meso-scale numerical procedure for

626 simulation of unreinforced masonry structures. Computers & Structures. 2013;120(0):9-23.

627 [23] Sarhosis V, Sheng Y. Identification of material parameters for low bond strength masonry.

628 Engineering Structures. 2014;60(0):100-10.

629 [24] Giamundo V, Sarhosis V, Lignola GP, Sheng Y, Manfredi G. Evaluation of different computational

630 modelling strategies for the analysis of low strength masonry structures. Engineering Structures.

631 2014;73(0):160-9.

632 [25] Lemos JV. Discrete element modeling of masonry structures. International Journal of

633 Architectural Heritage. 2007;1(2):190-213.

634 [26] Tumialan J, Morbin A, Nanni A, Modena C. Shear strengthening of masonry walls with FRP

635 composites. Composites. 2001:3-6.

636 [27] Diehl T. Modeling surface-bonded structures with ABAQUS cohesive elements: beam-type

637 solutions. ABAQUS User's Conference, Stockholm, Sweden2005.

638 [28] Nazir S, Dhanasekar M. Modelling the failure of thin layered mortar joints in masonry.

639 Engineering Structures. 2013;49(0):615-27.

640 [29] Haach VG, Vasconcelos G, Lourenço PB. Parametrical study of masonry walls subjected to in-

641 plane loading through numerical modeling. Engineering Structures. 2011;33(4):1377-89.

642 [30] Macorini L, Izzuddin B. A non‐linear interface element for 3D mesoscale analysis of brick‐

643 masonry structures. International Journal for Numerical Methods in Engineering. 2011;85(12):1584-

644 608.

645 [31] Su X, Yang Z, Liu G. Finite Element Modelling of Complex 3D Static and Dynamic Crack

646 Propagation by Embedding Cohesive Elements in Abaqus. Acta Mechanica Solida Sinica.

647 2010;23(3):271-82.

648 [32] Abaqus. Uer's Manual. Version 610.

649 [33] abaqus. Guidelines for Determining Finite Element Cohesive Material Parameters.

650 [34] Song K. Guidelines and Parameter Selection for the Simulation of Progressive Delamination.

651 2008 Abaqus Users' Conference. 2008.

652 [35] Yang W. Constitutive relationship model for masonry materials. Building Structure.

653 2009;38(10):80-2. (in Chinese)

654 [36] Zhen N. Research on Seismic Behavior of Masonry Structures with Fabricated tie-columns [D].

655 Chongqing: Chongqing University; 2010. (in Chinese)

656 [37] Li Z. Damage mechanics and applications Beijing: Science Press; 2002. (in Chinese)

657 [38] 3354-1999 GT. Test method for tensile properties of oriented fiber reinforced plastics. Beijing:

658 the Department of Supervision on Quality and Technology; 1999. (in Chinese)

659 [39] 50003-2011 G. Code for design of masonry structures. Chinese Architectural Industry Press.

660 Beijing: Chinese Architectural Industry Press; 2002. (in Chinese)

661 [40] GB50608-2010. Technical code for infrastructure application of FRP composites. Beijing:

662 Ministry of Construction of the People's Republic of China; 2011. (in Chinese)

663 [41] Tomazevic M. Earthquake-resistant design of masonry buildings: World Scientific Publishing

664 Company; 1999.

665 [42] Wang Q. Aseismatic shear strength of unreinforced masonry. Research Symposium of Masonry

666 Structure Changsha: Hunan University Press; 1989. p. 103-15. (in Chinese)

667 [43] Lesani M, Bahaari MR, Shokrieh MM. Numerical investigation of FRP-strengthened tubular T-

668 joints under axial compressive loads. Composite Structures. 2013;100(0):71-8.

669 [44] Sayed AM, Wang X, Wu Z. Finite element modeling of the shear capacity of RC beams

670 strengthened with FRP sheets by considering different failure modes. Construction and Building

671 Materials. 2014;59(0):169-79.

672 [45] Chandrasekharappa G, Srirangarajan HR. Parametric study of nonlinear static and dynamic

673 response of composite rectangular plates. Mechanics Research Communications. 1988;15(3):177-88.

674 [46] BS EN 1996-1-1: 2005 Eurocode 6: Design of masonry structures—General rules for reinforced

675 and unreinforced masonry structures.

676   [47] Zhuge Y. FRP-retrofitted URM walls under in-plane shear: review and assessment of available

677   models. Journal of Composites for Construction. 2010;14(6):743-53.

678   [48] Prota A, Manfredi G, Nardone F. Assessment of Design Formulas for In-Plane FRP Strengthening

679   of Masonry Walls. J Compos Constr. 2008;12(6):643-9.

680   [49] Lignola GP, Prota A, Manfredi G. Numerical investigation on the influence of FRP retrofit layout

681   and geometry on the in-plane behavior of masonry walls. Journal of Composites for Construction.

682   2012;16(6):712-23.